ACS NANO

www.acsnano.org

ARTICLE

Potassium Ammonium Vanadate with Rich Oxygen Vacancies for Fast and Highly Stable Zn-Ion Storage

Quan Zong, QianQian Wang, Chaofeng Liu, Daiwen Tao, Jiangying Wang,* Jingji Zhang, Huiwei Du, Junfu Chen, Qilong Zhang,* and Guozhong Cao*

Cite This: *ACS Nano* 2022, 16, 4588–4598

Read Online

ACCESS | Metrics & More | Article Recommendations | Supporting Information

ABSTRACT: **Vanadium-based materials have been extensively studied as promising cathode materials for zinc-ion batteries because of their multiple valences and adjustable ion-diffusion channels. However, the sluggish kinetics of Zn-ion intercalation and less stable layered structure remain bottlenecks that limit their further development. The present work introduces potassium ions to partially substitute ammonium ions in ammonium vanadate, leading to a subtle shrinkage of lattice distance and the increased oxygen vacancies. The resulting potassium ammonium vanadate exhibits a high discharge capacity (464 mAh g^{-1} at 0.1 A g^{-1}) and excellent cycling stability (90% retention over 3000 cycles at 5 A g^{-1}). The excellent electrochemical properties and battery performances are attributed to the rich oxygen vacancies. The introduction of K^+ to partially replace NH_4^+ appears to alleviate the irreversible deammoniation to prevent structural collapse during ion insertion/extraction. Density functional theory calculations show that potassium ammonium vanadate has a modulated electron structure and a better zinc-ion diffusion path with a lower migration barrier.**

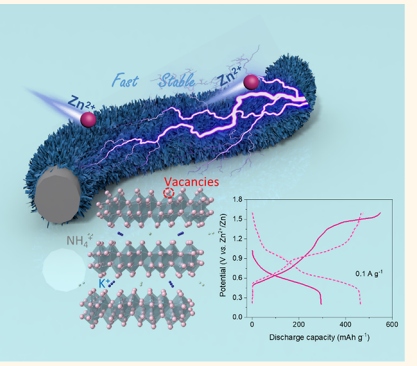

KEYWORDS: *ammonium vanadate, interlayer engineering, K^+ incorporation, oxygen vacancies, aqueous Zn-ion batteries*

Lithium-ion batteries (LIBs), as the most representative electrical energy storage (EES) system, have been intensively studied, and make up a huge market share in the past few decades.[1,2] However, lithium resources scarcity as well as flammable nature of lithium metal and organic electrolyte are two main inevitable issues in the future development and safe application of LIBs.[3,4] Aqueous zinc ion batteries (ZIBs) have attracted extensive attention owing to the advantages of metallic zinc anode including high theoretical capacity, low redox potential, and low cost as well as aqueous electrolytes with superior ionic conductivity (~1 S cm^{-1}) and nontoxicity.[5−7] Cathode materials allowing fast and reversible zinc ion (de)intercalation play an important role in the electrochemical performance of aqueous ZIBs. The development of cathode materials with a good balance between capacity, rate performance, and cycling stability remains a challenge.

Layered vanadium-based oxides have been widely employed as cathode materials for ZIBs due to the multiple valence states of V element and adjustable ion-transfer channels.[8−10] However, the unsatisfactory reaction kinetics and structure instability still hinder their commercial applications because of their low conductivity and narrow lattice spacing.[11−13] It is an effective strategy to incorporate molecules (H_2O), cations (such as Na^+, Mn^{2+}, Al^{3+}, NH_4^+, etc.), or polymers (PANI and PEDOT) into the [VO_n] layer to enlarge the interlayer spacing for rapid ion diffusion.[13−19] Among these foreign ions, ammonium vanadates have been developed as cathodes for zinc ion batteries by incorporating NH_4^+ into interlayers, such as $NH_4V_4O_{10}$, $(NH_4)_2V_7O_{16}$, and $(NH_4)_2V_6O_{16}{\cdot}1.5H_2O$, delivering high capacity (>350 mAh g^{-1} at 0.1 A g^{-1}) and a long cycle lifespan (>1000 cycles).[20−22] NH_4^+ possesses a large ionic radius (143 pm) and small molecular weight (18 g mol^{-1}), contributing to large interlayer spacing and high gravimetric capacities. NH_4^+ could also develop N−H···O hydrogen bonds with [VO_n] layers to ensure structural stability of the bilayers.[23,24] However, our previous work demonstrated that this hydrogen bond could be destroyed during a repeated charging/discharging process, recognized as the irreversible deammoniation, resulting in serious structural collapse.[25]

Received: December 15, 2021
Accepted: March 4, 2022
Published: March 8, 2022

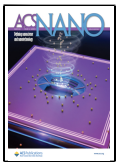

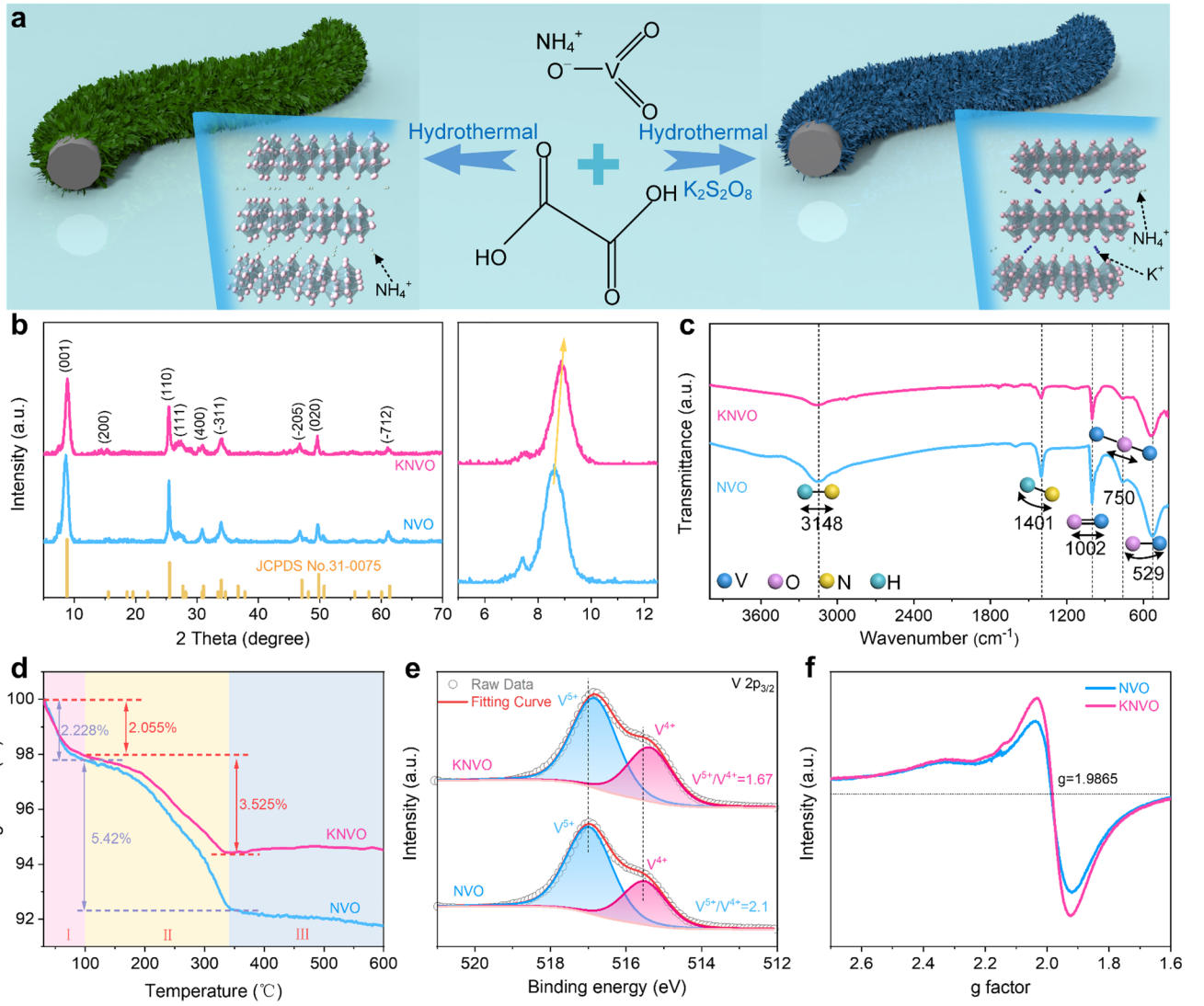

Figure 1. Phase and structural characterizations of NVO and KNVO. (a) Schematic illustration of the preparation process and the crystal structure. (b) XRD patterns. (c) FTIR spectra. (d) TG curves. (e) XPS spectra of V $2p_{3/2}$. (f) EPR spectra.

Alleviating the side effects caused by deammoniation is critical for the stable layered structure of ammonium vanadates (NVO).

Compared to ammonium ions, the monovalent alkaline metal cations could be introduced into the interlayer space to enhance ionic bonding, thus stabilizing the layered structure.[26] For example, Tian *et al.* incorporated K^+ into hydrated vanadium pentoxide, leading to a new phase ($KV_{12}O_{30-y}$·nH_2O, KVOH) with a contracted interlayer spacing.[27] KVOH exhibits better cycling stability than VOH because the introduction of K−O bonds with more ionic character (82%) and higher binding energy enhances the interaction between layers and stabilizes the crystal structure. However, the cations' pre-intercalated vanadates usually exhibit lowered theoretical capacity because of the reduction of pentavalent vanadium ions.[15] Defect engineering is an effective method to solve this problem because it can tune electronic structures to further improve the reaction kinetics and enhance the capacity.[28] In this regard, the effects of coupling ions' preintercalation and defect engineering should be taken into consideration when introducing guest ions into the host materials.

In this study, we report a substitution of partial ammonium ions by K^+ in the interlayer of $NH_4V_4O_{10}$ as a cathode for ZIBs. The resulting potassium ammonium vanadate (denoted as KNVO) shows a discharge capacity of 464 mAh g^{-1} at 0.1 A g^{-1} and retains a capacity of 189 mAh g^{-1} at 5 A g^{-1} after 3000 cycles. The outstanding electrochemical properties of KNVO are attributed to the rich oxygen vacancies promoting interfacial charge transfer and internal ion diffusion. The incorporation of K^+ appears to enhance the structural integrity and prevent irreversible deammoniation, thus resulting in long-term cycling stability.

RESULTS AND DISCUSSION

Figure 1a displays the synthesis process of NVO and KNVO nanoarrays on carbon cloth *via* a hydrothermal method. Only NH_4^+ ions occupy the space between the [VO_n] layer for the crystal structure of NVO, while K^+ and NH_4^+ coexist in the interlayer of KNVO. The XRD patterns of NVO, KNVO-1, KNVO, and KNVO-2 samples (synthesized by adding 0, 0.25, 0.5, and 1 mmol of $K_2S_2O_8$, respectively) are well indexed to a monoclinic $NH_4V_4O_{10}$ phase with a space group of *C*2/*m* (JCPDS no. 31-0075) in Figure 1b and Figure S1.[29] No

https://doi.org/10.1021/acsnano.1c11169
ACS Nano 2022, 16, 4588−4598

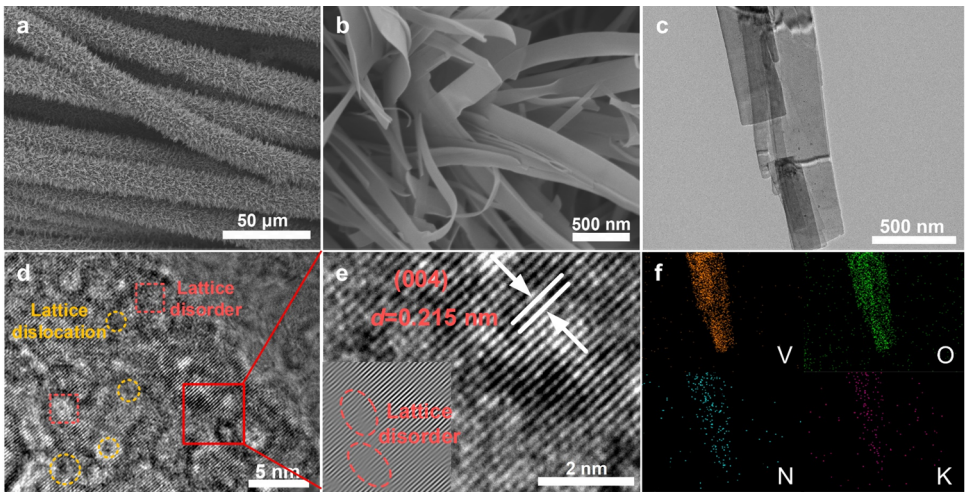

Figure 2. Morphology and structure of KNVO. (a,b) SEM images. (c−e) TEM and HRTEM images. Inset: corresponding IFFT images. (f) EDS mappings.

additional peaks related to any new phases are detected after the incorporation of K^+. The strong peak at 8.7° of NVO corresponds to the (001) plane with an interlayer spacing of 10.1 Å. After the substitution of NH_4^+ by K^+, the (001) peak slightly shifts toward a higher degree, indicating the shrinkage of interplanar spacing. As the concentration of K^+ increases, this (001) peak keeps moving to a higher degree (Figure S1). The slight decrease of lattice spacing in KNVO is possibly attributed to the small ion radius of K ions (133 pm of K^+ and 143 pm of NH_4^+) and the enhanced electrostatic interaction between K^+ and O^{2-}.[27] It is evident that the peak intensities of the KNVO are weaker than those of NVO, indicating the lower crystallinity after the potassium incorporation. ICP-OES analysis (Table S1) demonstrates that the atomic ratio of K to V in NVO, KNVO-1, KNVO, and KNVO-2 are 0:4, 0.17:4, 0.26:4, and 0.42:4, respectively. The FTIR spectra in Figure 1c further confirm the similar crystal structures of NVO and KNVO samples. The peak of 529 cm^{-1} is assigned to the bending mode of V−O, and a blue shift in KNVO is caused by oxygen vacancies. The peak located at 750 cm^{-1} is attributed to the antisymmetric V−O−V stretching mode.[30] The peak at 1002 cm^{-1} is a typical stretching vibration of V═O.[31] The peaks located at 1401 and 3148 cm^{-1} are attributed to the bending and stretching vibration of N−H bonds, respectively.[32] The peak intensity becomes weaker in KNVO due to the decrease of NH_4^+.

The TG curves of NVO and KNVO could be divided into three ranges (Figure 1d). The first stage (I) is the loss of physically adsorbed water, the second stage (II) is the loss of crystal water and ammonium ions, and the third range (III) is the complete loss of ammonium ions and the process of crystallization.[33] The total weight loss of KNVO and NVO is 5.58 and 7.65%, respectively. The lower total weight loss of KNVO compared to that of NVO is attributed to the residual K atoms after heat treatment, while the NH_4^+ ions are removed completely, supporting that the K ions are inserted into the ammonium vanadate. The survey XPS spectra of NVO and KNVO demonstrate the characteristic peaks of V 2p, O 1s, N 1s, and C 1s, and no signal of S could be observed in both samples (Figure S2). The K 2p XPS spectrum of KNVO exhibits two peaks, which can be ascribed to K $2p_{1/2}$ (295.2 eV) and K $2p_{3/2}$ (292.4 eV), while no K signal is detected in NVO (Figure S3).[34] For the high-resolution V $2p_{3/2}$ spectrum of NVO, the peak at 517.0 eV comes from V^{5+} and the signal at 515.6 eV is attributed to V^{4+}, respectively (Figure 1e). The characteristic peaks in KNVO shift to lower binding energies (516.9 eV for V^{5+} and 515.4 eV for V^{4+}) in comparison with NVO because the electron density of V is increased after the loss of adjacent oxygen atoms.[35,36] According to the fitted peak areas, the calculated V^{5+}/V^{4+} ratio of KNVO (1.67) is lower than that of NVO (2.1), indicating that partial V^{5+} ions are reduced to V^{4+} because more oxygen vacancies are formed after the introduction of K^+. The high-resolution O 1s spectrum of KNVO is fitted into three peaks at 529.5 (O1), 530.4 (O2), and 531.6 eV (O3), corresponding to lattice oxygen (V−O bonds), oxygen vacancies, and H_2O molecules, respectively (Figure S4).[37,38] The obviously stronger peak of oxygen vacancies in KNVO demonstrates that KNVO contains higher content of oxygen vacancies than NVO. The oxygen vacancies can be further confirmed by EPR because the signal originates from the unpaired electrons at the defect sites in an applied magnetic field.[39] V^{4+} is paramagnetic, while V^{5+} is EPR silent because of the integer spin; thus, the EPR intensity suggests the V^{4+} and oxygen vacancy state concentration.[9,40] As shown in Figure 1f, both the NVO and KNVO electrode show a strong signal of g = 1.9865, corresponding to the tetravalent V ion. Obviously, KNVO shows a higher signal intensity than that of NVO, demonstrating the increased V^{4+} content and decreased V^{5+} content because V^{5+} exhibits no EPR signal. The increased proportion of V^{4+} demonstrates that more oxygen vacancies are generated in KNVO, which is in accordance with the XPS results.

SEM and TEM images of KNVO (Figure 2a−c) show that the nanobelts are uniformly grown on the carbon fiber and the nanobelts are ultrathin. In addition, the morphology of KNVO is similar to that of NVO (Figure S5a,b), indicating that the incorporation of K would not change the morphology. The KNVO nanobelt shows a width of ∼250 nm, shorter than the ∼300 nm NVO nanobelt. Moreover, the width of the nanobelts became smaller with increasing K^+ content (Figure S5c−f), which is possibly attributed to the slower growth rate affected by K along the direction of width. The high-resolution TEM (HRTEM) image in Figure 2d displays various lattice disorders and lattice dislocations, which are caused by oxygen vacancies. The corresponding selected area electron diffraction (SAED) pattern reveals the single-crystalline nature of KNVO

https://doi.org/10.1021/acsnano.1c11169
ACS Nano 2022, 16, 4588−4598

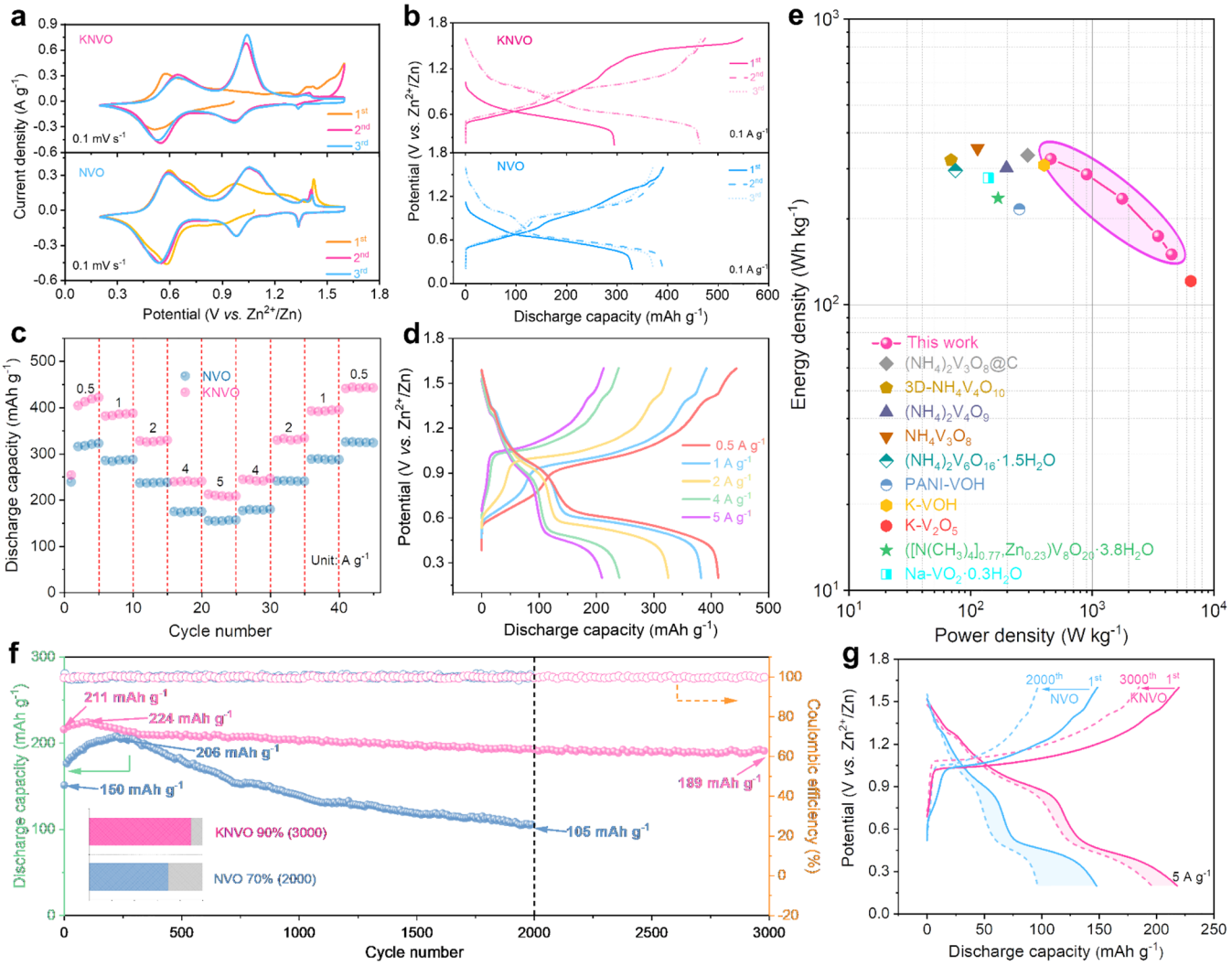

Figure 3. Electrochemical properties of KNVO and NVO electrodes. (a) CV curves at 0.1 mV s^{-1} and (b) voltage profiles at 0.1 A g^{-1} in the first three cycles. (c) Discharge capacity and (d) voltage profiles at different current densities. (e) Ragone plot. (f) Cycling performance at 5 A g^{-1}. (g) Voltage profiles before and after cycling.

(Figure S6). The measured interplanar spacing of 0.218 nm in NVO (Figure S7) is attributed to the (004) plane, decreased to 0.215 nm for KNVO (Figure 2e), which is in accordance with the result of XRD. The corresponding inverse Fast fourier transform (IFFT) image further confirms the lattice disorder. EDS mappings in Figure 2f demonstrate that the V, O, N, and K elements are distributed uniformly throughout the whole nanobelt, while NVO only shows V, O, and N elements (Figure S8), further proving the successful insertion of K^+ into NVO.

The first three-cycle CV curves of KNVO and NVO at 0.1 mV s^{-1} are compared in Figure 3a. The sharp curve at high voltage in the first cycle of KNVO corresponds to the *in situ* electrochemical oxidation of V^{4+} because of the higher content of V^{4+} than that of NVO according to XPS results. The overlapped CV curves indicate the reversible redox reaction and the redox peaks at ~1 V (V^{5+}/V^{4+}) and ~0.6 V (V^{4+}/V^{3+}) are the same as those for the reported ions in pre-intercalated vanadium oxides.[41,42] In addition, the small redox peaks at ~1.35 V could be possibly assigned to the NH_4^+ (de)-intercalation. The weakened redox peaks in KNVO suggest that K-incorporation could alleviate the irreversible deammoniation.[43] Figure 3b compares the first three-cycle voltage plots of KNVO and NVO at 0.1 A g^{-1}. The first charge curve of KNVO exhibits a plateau at around 1.4 V, suggesting the electrochemical oxidation of V^{4+} to V^{5+}, consistent with the anodic peak in the first CV curve. The KNVO shows a lower discharge capacity than NVO in the first cycle because of the lower ratio of V^{5+} to V^{4+}. The subsequent discharge plots show two plateaus at ~1.0 and ~0.6 V, which are in accordance with the redox peak positions of the CV curves, indicating a two-step intercalation process of Zn^{2+}. The highly overlapped charging/discharging profiles of KNVO demonstrate that the KNVO electrode displays better reversibility than NVO. In addition, the KNVO electrode delivers a discharge capacity of 464 mAh g^{-1} at 0.1 A g^{-1}, higher than that of NVO (391 mAh g^{-1}), KNVO-1 (408 mAh g^{-1}), and KNVO-2 (433 mAh g^{-1}) (Figure S9a,b). Because of the electrochemical oxidation process, the discharge capacity of K-incorporated ammonium vanadate (KNVO, KNVO-1, and KNVO-2) gradually increases in the first five cycles at 0.5 A g^{-1}, and the KNVO electrode exhibits higher capacities than NVO, KNVO-1, and KNVO-2 at the same current densities (Figure 3c and Figure S9c). The average discharge capacities of KNVO at 0.5, 1, 2, 4, and 5 A

https://doi.org/10.1021/acsnano.1c11169
ACS Nano 2022, 16, 4588−4598

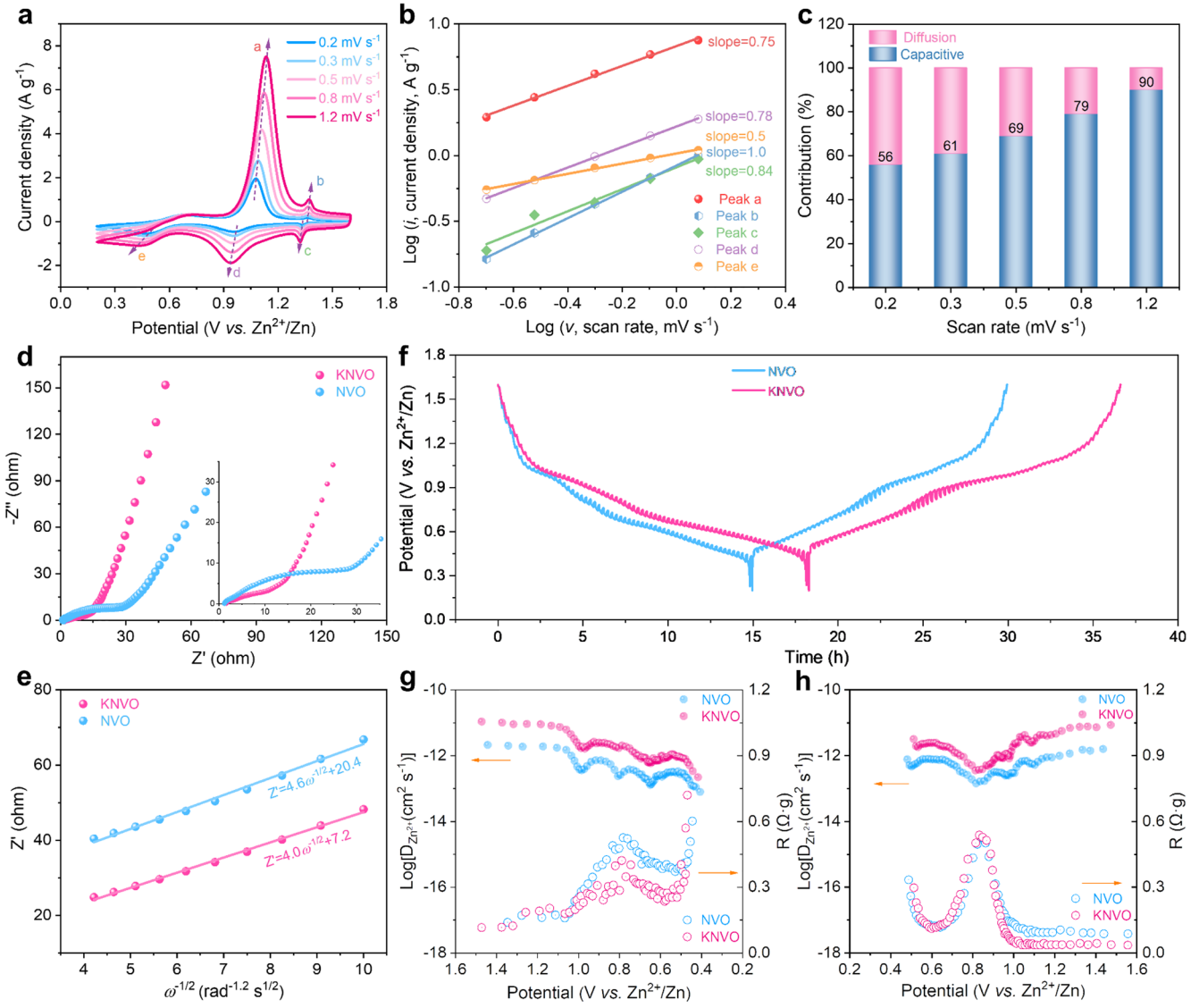

Figure 4. Electrochemical reaction kinetics of two samples. (a) CV curves at different scan rates. (b) Relationship between peak currents and scan rates. (c) Capacitive contributions of KNVO at different scan rates. (d) Nyquist plot. (e) Relationship between the real part of impedance and low frequencies. (f) GITT plot at 0.05 A g^{-1}. (g,h) Zn ion diffusion coefficients and reaction resistance calculated from GITT plot.

g^{-1} are 422, 383, 325, 240, and 210 mAh g^{-1}, respectively, demonstrating an excellent rate performance, and the corresponding voltage profiles are shown in Figure 3d. When the current density decreases to 0.5 A g^{-1}, the capacity could be recovered to 440 mAh g^{-1}, indicating good reversibility. In addition, a high energy density of 324 Wh kg^{-1} could be achieved at a power density of 457 W kg^{-1}, higher than the recently reported ammonium vanadates and pre-intercalated vanadium oxides, as shown in the Ragone plot (Figure 3e).[21,27,30,44−49] Even at a high power output of 4500 W kg^{-1}, the KNVO electrode delivers a high energy density of 150 Wh kg^{-1}. As shown in Figure 3f, the KNVO electrode delivers an initial discharge capacity of 211 mA h g^{-1} at 5 A g^{-1}, achieves a maximum capacity of 224 mAh g^{-1} after 100 cycles, and retains a stable capacity of 189 mAh g^{-1} after 3000 cycles. In comparison, the NVO electrode shows rapid capacity decay after reaching the maximum capacity of 206 mAh g^{-1}, and only 70% capacity retention is retained after 2000 cycles at the same current density. In addition, both of them show an increase in discharge capacity in the initial 200 cycles, which is caused by an activation process due to the incomplete extraction of Zn^{2+} acting as "pillars" in the interlayer to further enhance the capacity.[50] The overall capacity retention of KNVO (90%) is also higher than that of KNVO-1 (77%) and KNVO-2 (80%) after 3000 cycles (Figure S9d). The voltage profiles of KNVO and NVO before and after cycling are compared in Figure 3g. The large capacity decay at low voltage of NVO is due to the degradation of the structure caused by deammoniation, which makes it difficult for zinc ion insertion/extraction. The capacity decay of KNVO mainly originates from the first discharge plateau, which could be possibly attributed to the decreased space for the insertion of large-sized ions as discussed later. The excellent cycling stability of KNVO could be possibly attributed to the prevention of irreversible deammoniation after the partial substitution of NH_4^+ by K^+. The crystal structure and morphology of the KNVO electrode before and after cycling were further studied by XRD and SEM. The XRD patterns demonstrate that the phase of KNVO electrode is well

https://doi.org/10.1021/acsnano.1c11169
ACS Nano 2022, 16, 4588−4598

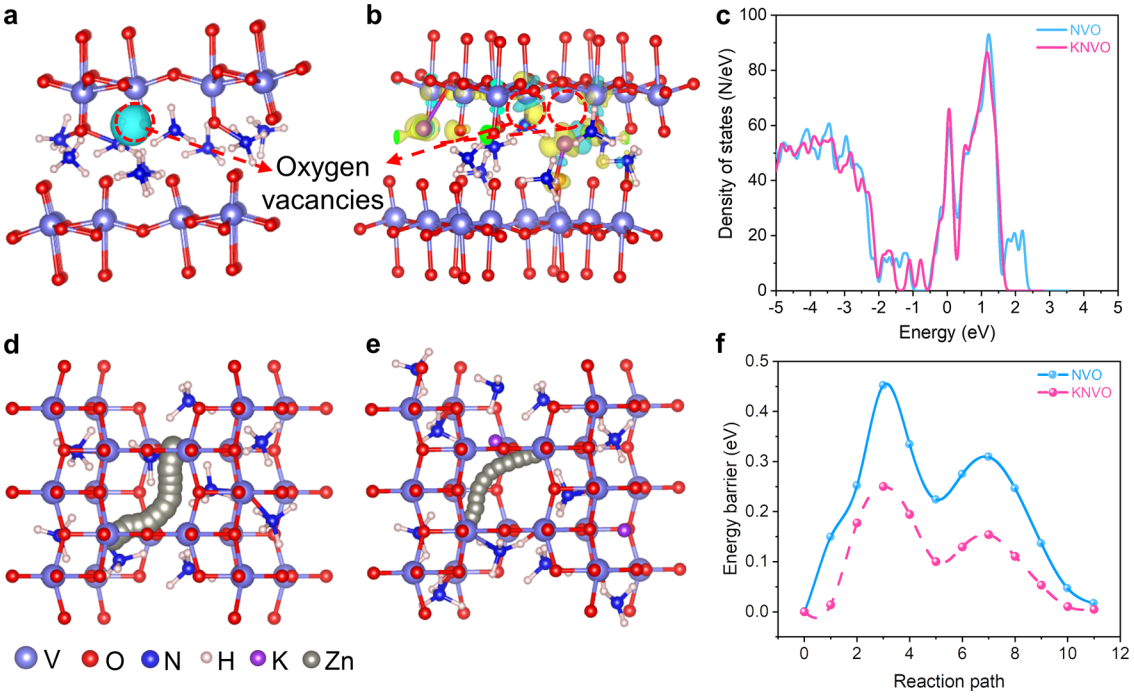

Figure 5. First-principle calculations results. Charge density difference analysis of (a) NVO and (b) KNVO. (c) Density of states of NVO and KNVO. Possible migration pathways for Zn^{2+} in (d) NVO and (e) KNVO. (f) Calculated Zn^{2+} diffusion barriers for paths in the NVO and KNVO.

maintained without generation of other new phases (Figure S10). SEM images also reveal that the KNVO sample maintains the initial nanobelt morphology (Figure S11). The electrochemical properties of the KNVO electrode are superior to those of many reported vanadium-based cathodes as shown in Table S2.

To study the electrochemical kinetics of the KNVO electrode, CV curves at different scan rates were measured (Figure 4a). The slight peak shift is attributed to the polarization during Zn^{2+} intercalation/deintercalation. The relationship of peak current (i) and scan rate (v) could be described by the equation $i = av^b$, where a and b are adjustable parameters.[42,51] A b value of 1 suggests a surface capacitive behavior, while b = 0.5 represents a diffusion-controlled process. The b values of peaks a−e are determined as 0.75, 1, 0.84, 0.78, and 0.5 by fitting the log(i) versus log(v) curve, respectively, demonstrating that the charge storage process is controlled by both diffusion and capacitive behavior (Figure 4b). The larger b values of KNVO suggest the faster ion diffusion kinetics compared with those of NVO (Figure S12). The ratios of the capacitive (k_1v) and diffusion-controlled (k_2v) contributions can be approximately calculated on the basis of the equations $i = k_1v + k_2v^{1/2}$ and $i/v^{1/2} = k_1v^{1/2} + k_2$.[52] With the increase of scan rates from 0.2 to 1.2 mV s^{-1}, the proportion of capacitance increases from 56% to 90% (Figure 4c). This result suggests that the reaction process of KNVO is mainly controlled by the surface capacitive behavior at a high scan rate. The ratio of capacitive process in KNVO is higher than that of NVO at the same scan rate (Figure S13), demonstrating that the oxygen vacancies induce ion absorption reaction, thus contributing to an excellent rate performance. In addition, Nyquist plots of KNVO and NVO after 15 cycles of CV tests (Figure 4d) are fitted to investigate the charge-transfer resistance and ion-diffusion coefficients. The diameter of the semicircle in the high-frequency region is related to the charge-transfer resistance (R_{ct}). The KNVO electrode shows obviously lower R_{ct} (12.6 Ω) than that of NVO (32 Ω), which suggests fast surface electron mobility for KNVO. The Zn ion diffusion coefficients ($D_{Zn^{2+}}$) are obtained from the relationship between low frequencies ($\omega^{-1/2}$) and the real part of impedance (Z') in Figure 4e (details shown in the Supporting Information).[7,53] The KNVO electrode presents a higher $D_{Zn^{2+}}$ of 9.6×10^{-13} cm^2 s^{-1} than that of NVO (7.3×10^{-13} cm^2 s^{-1}), demonstrating the improved ion-transfer kinetics due to oxygen vacancies facilitating the ion diffusion.

GITT measurements were also carried out to estimate the internal reaction resistance (RR) and $D_{Zn^{2+}}$ of two electrodes throughout the entire charge−discharge process (Figure 4f−h; calculation details are described in the Supporting Information).[16,34,54] The KNVO displays higher $D_{Zn^{2+}}$ and lower RR than those of NVO, and the calculated $D_{Zn^{2+}}$ of KNVO and NVO are between 10^{-13} and 10^{-11} cm^2 s^{-1}, consistent with EIS results. Generally, Zn^{2+} exists in the aqueous electrolyte in the form of $[Zn(H_2O)_6]^{2+}$ with a large size of 2.1 Å.[55] Before being discharged to 1.1 V, the RRs are lower than 0.2 Ω·g and the $D_{Zn^{2+}}$ remains stable because the interlayer distance is large enough for the insertion of $[Zn(H_2O)_6]^{2+}$. When discharged to 0.8 V, it is difficult for $[Zn(H_2O)_6]^{2+}$ to insert into the interlayer space, resulting in the gradual increase of RR values and the decrease of $D_{Zn^{2+}}$. Then the RR values go down in the range of 0.8−0.5 V owing to the further insertion of small-sized Zn^{2+}, which originates from the desolvation of $[Zn(H_2O)_6]^{2+}$. After 0.5 V, the dramatic increase of RRs suggests the difficult diffusion of Zn^{2+} because no channels are available for any ion intercalation. The discharging process of KNVO involves the successive insertion/extraction of hydrated zinc ions and zinc ions, which is consistent with the two plateaus in the voltage profile. *Ex situ* O 1s XPS spectra further confirm the ions intercalation process of KNVO (Figure S14). When discharged to 0.8 V, the content of water increases to 80%, indicating the

https://doi.org/10.1021/acsnano.1c11169
ACS Nano 2022, 16, 4588−4598

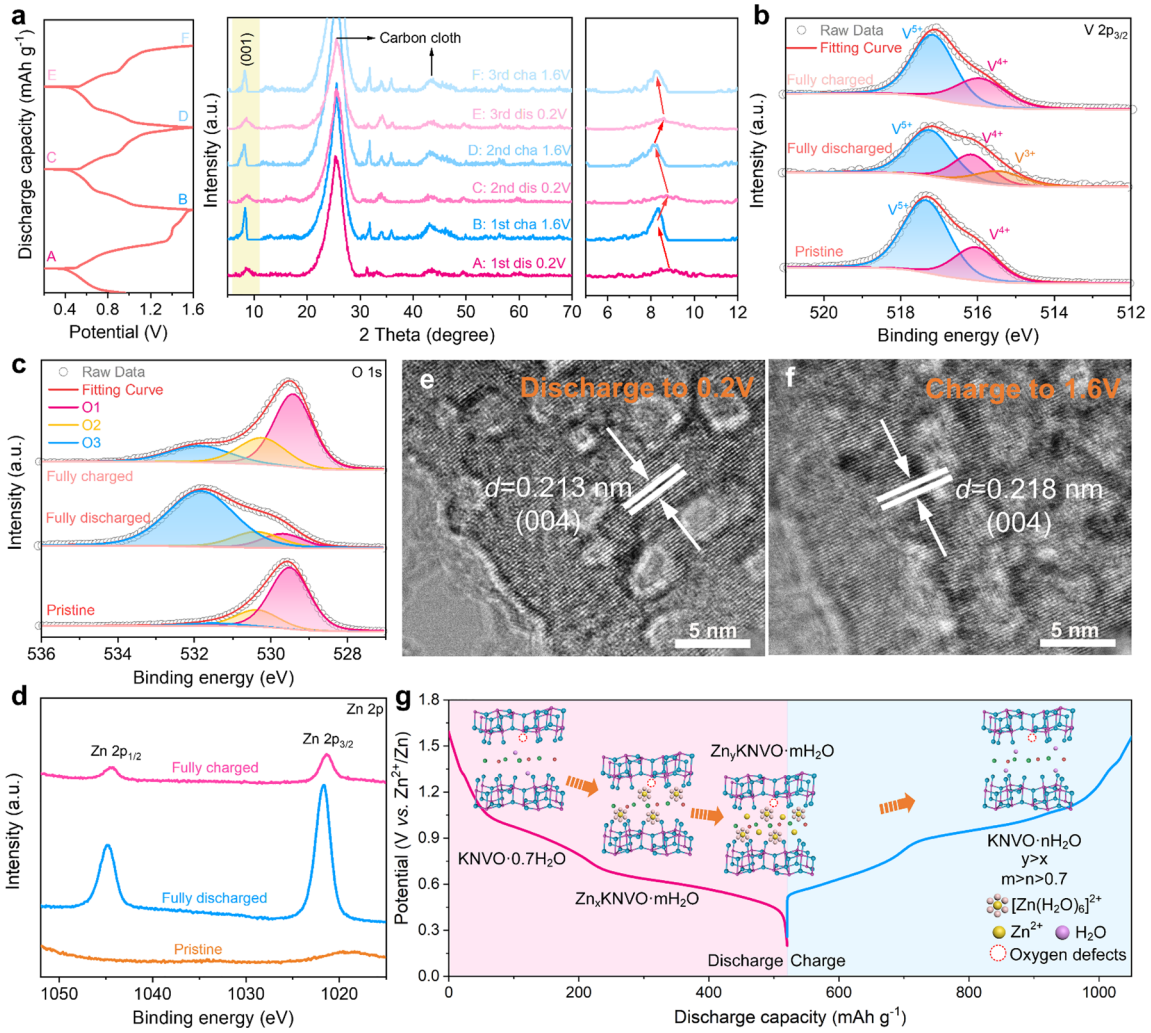

Figure 6. Charge storage mechanism of KNVO. (a) *Ex situ* XRD patterns in the first three cycles. *Ex situ* XPS spectra (b) V 2p, (c) O 1s, and (d) Zn 2p. *Ex situ* HRTEM images at (e) fully discharged state and (f) fully charged state. (g) Schematic illustrations of Zn^{2+} storage mechanism of KNVO.

insertion of $[Zn(H_2O)_6]^{2+}$ and remains stable after 0.8 V, suggesting the insertion of Zn^{2+}. In the charging process, the high RR values around 0.8 V are possibly attributed to the phase transformation during the extraction of zinc ions.

Density functional theory (DFT) calculations were conducted to clarify the impacts of K ions and oxygen vacancies and reveal the diffusion pathway and diffusion energy barriers of zinc ions in NVO and KNVO. Charge density difference analysis of NVO and KNVO was performed (Figure 5a,b) to demonstrate the modulation of electron structure after the incorporation of K ions. The negative charge distribution shifts toward the V atoms due to more oxygen vacancies, resulting in the weak electrostatic interaction between zinc ions and $[VO_n]$ layers during the intercalation of zinc ions, thereby facilitating the diffusion kinetics. In addition, K^+ develops a strong chemical bond with O^{2-}, which ensures the structural stability. The density of state (DOS) results (Figure 5c) show that KNVO displays a new electronic state and higher density state near the Fermi level, suggesting an enhanced conductivity, which is beneficial to electron transfer during redox reactions, thus contributing to high capacity.[56] The top and side views of possible migration pathways for Zn^{2+} in NVO and KNVO are shown in Figure 5d,,e and S16, where Zn^{2+} mainly diffuses along the *b* axis as reported in many similar works.[7,57] The energy barrier along the Zn^{2+} migration pathways for KNVO is approximately 0.25 eV in Figure 5f, lower than that of NVO (~0.46 eV) and previously reported vanadium oxides, suggesting K ions and oxygen vacancies optimize the pathway and promote a faster Zn^{2+} migration.[28,42,57]

The charge-storage mechanism of KNVO during the charging/discharging process was further studied *via* multiple *ex situ* characterizations. The *ex situ* XRD patterns of the first three cycles are shown in Figure 6a. No additional new peaks are detected at the fully charge/discharge states compared to the pristine electrode, demonstrating that the intercalated Zn ions do not lead to the generation of new phases. As shown in the enlarged XRD pattern, the diffraction peak of the (001) reflection shifts slightly to higher angles at the fully discharged state, indicating a contraction of lattice spacing from 9.9 to 9.6 Å. The decrease of lattice spacing is possibly attributed to an increased electrostatic interaction within the bilayers because of the intercalation of Zn^{2+}. After charging to 1.6 V, the (001) reflection returns to its original position with the extraction of Zn^{2+}, demonstrating the reversible structure of the KNVO electrode during the Zn ions intercalation/deintercalation.

https://doi.org/10.1021/acsnano.1c11169
ACS Nano 2022, 16, 4588−4598

Ex situ XPS spectra are presented in Figure 6b–d. Compared to the pristine electrode, the intensity of V^{5+} shows an apparent decrease and a new peak located at 515.4 eV is ascribed to V^{3+} at the fully discharged state, which is associated with the reduction of V^{5+} and V^{4+} during the Zn^{2+} intercalation process.[58,59] The contents of vanadium ions with different valence are inaccurate because trivalent vanadium ions are easily reduced during the *ex situ* XPS characterization. At the fully charged state, the V^{4+} and V^{3+} are reversibly oxidized to V^{5+}. For the O 1s *ex situ* XPS spectra (Figure 6c), the intensity of O1 decreases in the discharging process and then recovers during charging. The intensity of O2 peak shows a decrease when discharging to 0.2 V, indicating the decrease of the content of oxygen vacancies. This is because the oxygen vacancies could be filled by the O^{2-} from water with the intercalation of Zn^{2+} and water during the discharge process.[60] The lower EPR intensity of the fully discharged electrode further confirms the lower oxygen vacancy concentration (Figure S17). The intensity of O_3 (water molecule) becomes stronger at the fully discharged state due to the insertion of $[Zn(H_2O)_6]^{2+}$. After charging to 1.6 V, the decreased intensity of the O_3 peak indicates that most of the H_2O molecules coordinated with zinc ions are extracted from the layer, while the residual H_2O stay in the interlayer as crystal water compared to the pristine electrode. As shown in Figure 6d, no Zn signal is detected at the pristine state. After being discharged to 0.2 V, the Zn 2p spectrum shows two strong characteristic peaks of Zn $2p_{1/2}$ (1044.8 eV) and Zn $2p_{3/2}$ (1021.7 eV), respectively, confirming the successful insertion of Zn ions into the KNVO electrode.[61] At the fully charged state, the weak intensity of the Zn 2p peaks indicates that most zinc ions are de-intercalated from the KNVO and the residual zinc ions originate from the absorbed Zn^{2+} or Zn^{2+} existing in the crystal lattice.

The morphology of the KNVO electrode demonstrates no obvious change during the charge–discharge process from the *ex situ* TEM images (Figure S18). The HRTEM image of the electrode discharged to 0.2 V in Figure 6e displays a lattice distance of 0.213 nm, which matches a shrinkage (004) crystal lattice plane of monoclinic $NH_4V_4O_{10}$ phase. When charged to 1.6 V, the interplanar spacing of the (004) crystal plane recovers to 0.218 nm due to the deintercalation of Zn^{2+} ions (Figure 6f). EDS mappings (Figure S19) display the V, O, N, K, and Zn elements distributed in the fully discharged/charged electrode. The different intensities of Zn signals illustrate the reversible Zn ion insertion/extraction. The detected signal of Zn in the fully charged electrode corresponds to the lattice-trapped Zn ions or absorbed Zn ions on the surface, consistent with the *ex situ* XPS results. The K and N elements are detected in both states, implying that K^+ and NH_4^+ stay stable in the interlayer spacing. Obviously, the HRTEM and EDS analyses also confirm the reversible Zn^{2+} storage in the KNVO cathode. On the basis of the analysis of electrochemical reaction kinetics and *ex situ* characterizations, the possible charge-storage mechanism is illustrated in Figure 6g. Throughout the charge/discharge, KNVO electrode experiences the reversible insertion/extraction of $[Zn(H_2O)_6]^{2+}$ and Zn^{2+} with no side reactions. The rich oxygen vacancies permit the fast ion diffusion, and the proper K^+ and NH_4^+ cations in the interlayer space could stabilize the layered structure.

CONCLUSIONS

Potassium ammonium vanadate nanobelts with rich oxygen vacancies exhibits outstanding electrochemical properties as a cathode material for aqueous ZIBs. The KNVO electrode delivers an enhanced capacity, excellent rate capability, and outstanding cycling stability. Experimental data and calculations reveal that the oxygen vacancies and K cations could optimize the diffusion path and reduce the diffusion barrier, permitting fast and reversible Zn^{2+} (de)intercalation. The incorporation of potassium appears to alleviate the irreversible deammoniation, thus ensuring the stability of whole structure. The *ex situ* characterizations demonstrate a reversible $[Zn(H_2O)_6]^{2+}/Zn^{2+}$ insertion/extraction process without phase transition. This work could provide a promising ammonium vanadate as a high-performance cathode for emerging aqueous ZIBs and multivalent metal-ion batteries.

MATERIALS AND METHODS

Synthesis of K-Incorporated Ammonium Vanadate (KNVO). All chemicals were used without further purification. The carbon cloth was cleaned by HCl, acetone, deionized water, and absolute ethanol, respectively. NH_4VO_3 (4 mmol) and of $H_2C_2O_4{\cdot}2H_2O$ (4.8 mmol) were dissolved into 80 mL of DI water with stirring for 30 min. Then, 0.5 mmol of $K_2S_2O_8$ was added into the above solution and stirred for another 10 min. The mixture with a piece of carbon cloth was then heated and maintained at 180 °C for 6 h. After the reaction, the carbon cloth was rinsed by ethanol and DI water three times. The KNVO material grown on carbon cloth was obtained after dryingd at 60 °C for 12 h in a vacuum oven. The mass loading of KNVO was approximately 1.2 mg cm^{-2}. For comparison, 0, 0.25, and 1 mmol of $K_2S_2O_8$ was used to prepare three additional samples, denoted as NVO, KNVO-1, and KNVO-2, respectively.

Characterizations. Phase characterizations were investigated by XRD with Cu Kα radiation (Rigaku, D/Ultima IV, λ = 1.5418 Å). TG-DSC (Netzsch 449 F3) was conducted with a 10 °C min^{-1} heating rate in air from 30 to 600 °C. The compositional evolution and surface valence states were investigated by XPS (Thermo Fisher Scientific, Kalpha). ICP-OES analysis was employed to acquire the exact composition. EPR (Bruker A300) measurements were used to study the oxygen vacancies. SEM (SU-8010) and TEM (Tecnai G2 F20) with an EDS were used to analyze the morphology and structure of samples.

Electrochemical Measurements. CR2032 coin-type cells were assembled in air using as-prepared samples, Zn plate, 80 μL of 3 M $Zn(CF_3SO_3)_2$, and a glass fiber filter (Whatman, grade 934-AH) as the cathode, anode, electrolyte, and separator, respectively. Cyclic voltammetry (CV) and electrochemical impedance spectroscopy (EIS) were obtained on an electrochemical workstation (CHI 760E). The galvanostatic charge–discharge and galvanostatic intermittent titration technique (GITT) were recorded on a battery testing system (Neware, CT-4008).

Computational Method. Density functional theory calculations were performed using the Vienna Ab initio Simulation Package based on the pseudopotential plane wave method.[62] The Perdew–Bueke–Ernzerhof functional was used to describe exchange-correlation effects of electrons. The projected augmented wave potentials were chosen to describe the ionic cores and take valence electrons into account using a plane wave basis set with a kinetic energy cutoff of 500 eV.[58] In this calculation, two different configurations containing either an O-vacancy or K ion were considered. During the geometry optimizations, all of the atom positions were allowed to relax. The Brillouin-zone sampling was conducted using Monkhorst–Pack grids of special points with a separation of 0.04 $Å^{-1}$. The convergence criterion for the electronic self-consistent field loop was set to 10^{-5} eV/atom. The atomic structures were optimized until the residual forces were below 0.05 eV $Å^{-1}$. In order to investigate the diffusion properties for Zn ion, the CI-NEB method was employed.[63]

https://doi.org/10.1021/acsnano.1c11169
ACS Nano 2022, 16, 4588–4598

ASSOCIATED CONTENT

Supporting Information

The Supporting Information is available free of charge at https://pubs.acs.org/doi/10.1021/acsnano.1c11169.

XRD patterns, XPS spectra, SEM and TEM images of NVO, KNVO, KNVO-1, and KNVO-2; electrochemical properties of KNVO-1 and KNVO-2; XRD and SEM of KNVO before and after cycling; $\log(i)$ *vs* $\log(v)$ plot and capacitive contributions of NVO; *ex situ* O 1s XPS spectra; GITT profiles; side view of migration pathways for Zn^{2+}; EPR spectra, TEM images, and EDS mappings of KNVO at fully discharged/charged states (PDF)

AUTHOR INFORMATION

Corresponding Authors

Jiangying Wang − *College of Materials and Chemistry, China Jiliang University, Hangzhou 310018 Zhejiang, People's Republic of China*; Email: wangjiangying@cjlu.edu.cn

Qilong Zhang − *School of Materials Science and Engineering, Zhejiang University, Hangzhou 310027 Zhejiang, People's Republic of China*; orcid.org/0000-0003-1191-5946; Email: mse237@zju.edu.cn

Guozhong Cao − *Department of Materials Science and Engineering, University of Washington, Seattle, Washington 98195, United States*; orcid.org/0000-0001-6539-0490; Email: gzcao@uw.edu

Authors

Quan Zong − *College of Materials and Chemistry, China Jiliang University, Hangzhou 310018 Zhejiang, People's Republic of China*

QianQian Wang − *School of Science, Huzhou University, Huzhou 313000 Zhejiang, People's Republic of China*

Chaofeng Liu − *Department of Materials Science and Engineering, University of Washington, Seattle, Washington 98195, United States*

Daiwen Tao − *School of Materials Science and Engineering, Zhejiang University, Hangzhou 310027 Zhejiang, People's Republic of China*

Jingji Zhang − *College of Materials and Chemistry, China Jiliang University, Hangzhou 310018 Zhejiang, People's Republic of China*

Huiwei Du − *College of Materials and Chemistry, China Jiliang University, Hangzhou 310018 Zhejiang, People's Republic of China*

Junfu Chen − *College of Materials and Chemistry, China Jiliang University, Hangzhou 310018 Zhejiang, People's Republic of China*

Complete contact information is available at: https://pubs.acs.org/10.1021/acsnano.1c11169

Notes

The authors declare no competing financial interest.

ACKNOWLEDGMENTS

This work was supported by the Science and Technology Program of Guangxi Zhuang autonomous region (Grant No. ZD20302001) and basic public welfare research program of Zhejiang Province (LQ20E070003). The authors also acknowledge financial support from startup capital at atChina Jiliang University (No. 210943).

REFERENCES

(1) Jia, X.; Liu, C.; Neale, Z. G.; Yang, J.; Cao, G. Active Materials for Aqueous Zinc Ion Batteries: Synthesis, Crystal Structure, Morphology, and Electrochemistry. *Chem. Rev.* **2020**, *120*, 7795−7866.

(2) Fan, E.; Li, L.; Wang, Z.; Lin, J.; Huang, Y.; Yao, Y.; Chen, R.; Wu, F. Sustainable Recycling Technology for Li-Ion Batteries and Beyond: Challenges and Future Prospects. *Chem. Rev.* **2020**, *120*, 7020−7063.

(3) Blanc, L. E.; Kundu, D.; Nazar, L. F. Scientific Challenges for the Implementation of Zn-Ion Batteries. *Joule* **2020**, *4*, 771−799.

(4) Yong, B.; Ma, D.; Wang, Y.; Mi, H.; He, C.; Zhang, P. Understanding the Design Principles of Advanced Aqueous Zinc-Ion Battery Cathodes: From Transport Kinetics to Structural Engineering, and Future Perspectives. *Adv. Energy Mater.* **2020**, *10*, 2002354.

(5) Liang, Y.; Dong, H.; Aurbach, D.; Yao, Y. Current Status and Future Directions of Multivalent Metal-Ion Batteries. *Nat. Energy* **2020**, *5*, 646−656.

(6) Kundu, D.; Adams, B. D.; Duffort, V.; Vajargah, S. H.; Nazar, L. F. A High-Capacity and Long-Life Aqueous Rechargeable Zinc Battery Using a Metal Oxide Intercalation Cathode. *Nat. Energy* **2016**, *1*, 16119.

(7) Zhu, K.; Wu, T.; Huang, K. $NaCa_{0.6}V_6O_{16}{\cdot}3H_2O$ as an Ultra-Stable Cathode for Zn-Ion Batteries: The Roles of Pre-Inserted Dual-Cations and Structural Water in V_3O_8 Layer. *Adv. Energy Mater.* **2019**, *9*, 1901968.

(8) Liu, S.; Kang, L.; Kim, J. M.; Chun, Y. T.; Zhang, J.; Jun, S. C. Recent Advances in Vanadium-Based Aqueous Rechargeable Zinc-Ion Batteries. *Adv. Energy Mater.* **2020**, *10*, 2000477.

(9) Li, Z.; Ren, Y.; Mo, L.; Liu, C.; Hsu, K.; Ding, Y.; Zhang, X.; Li, X.; Hu, L.; Ji, D.; Cao, G. Impacts of Oxygen Vacancies on Zinc Ion Intercalation in VO_2. *ACS Nano* **2020**, *14*, 5581−5589.

(10) Deng, S.; Yuan, Z.; Tie, Z.; Wang, C.; Song, L.; Niu, Z. Electrochemically Induced Metal-Organic-Framework-Derived Amorphous V_2O_5 for Superior Rate Aqueous Zinc-Ion Batteries. *Angew. Chem., Int. Ed.* **2020**, *59*, 22002−22006.

(11) Liang, X.; Yan, L.; Li, W.; Bai, Y.; Zhu, C.; Qiang, Y.; Xiong, B.; Xiang, B.; Zou, X. Flexible High-Energy and Stable Rechargeable Vanadium-Zinc Battery Based on Oxygen Defect Modulated V_2O_5 Cathode. *Nano Energy* **2021**, *87*, 106164.

(12) Song, M.; Tan, H.; Chao, D.; Fan, H. J. Recent Advances in Zn-Ion Batteries. *Adv. Funct. Mater.* **2018**, *28*, 1802564.

(13) Yan, M.; He, P.; Chen, Y.; Wang, S.; Wei, Q.; Zhao, K.; Xu, X.; An, Q.; Shuang, Y.; Shao, Y.; Mueller, K. T.; Mai, L.; Liu, J.; Yang, J. Water-Lubricated Intercalation in $V_2O_5{\cdot}nH_2O$ for High-Capacity and High-Rate Aqueous Rechargeable Zinc Batteries. *Adv. Mater.* **2018**, *30*, 1703725.

(14) Zhao, H.; Fu, Q.; Yang, D.; Sarapulova, A.; Pang, Q.; Meng, Y.; Wei, L.; Ehrenberg, H.; Wei, Y.; Wang, C.; Chen, G. In Operando Synchrotron Studies of NH_4^+ Preintercalated $V_2O_5{\cdot}nH_2O$ Nanobelts as the Cathode Material for Aqueous Rechargeable Zinc Batteries. *ACS Nano* **2020**, *14*, 11809−11820.

(15) Zhang, G.; Wu, T.; Zhou, H.; Jin, H.; Liu, K.; Luo, Y.; Jiang, H.; Huang, K.; Huang, L.; Zhou, J. Rich Alkali Ions Preintercalated Vanadium Oxides for Durable and Fast Zinc-Ion Storage. *ACS Energy Lett.* **2021**, *6*, 2111−2120.

(16) Liu, C.; Neale, Z.; Zheng, J.; Jia, X.; Huang, J.; Yan, M.; Tian, M.; Wang, M.; Yang, J.; Cao, G. Expanded Hydrated Vanadate for High-Performance Aqueous Zinc-Ion Batteries. *Energy Environ. Sci.* **2019**, *12*, 2273−2285.

(17) Liu, S.; Zhu, H.; Zhang, B.; Li, G.; Zhu, H.; Ren, Y.; Geng, H.; Yang, Y.; Liu, Q.; Li, C. C. Tuning the Kinetics of Zinc-Ion Insertion/Extraction in V_2O_5 by In Situ Polyaniline Intercalation Enables Improved Aqueous Zinc-Ion Storage Performance. *Adv. Mater.* **2020**, *32*, 2001113.

(18) Wei, T.; Liu, Y.; Yang, G.; Wang, C. Aluminum Vanadate Hollow Spheres as Zero-Strain Cathode Material for Highly Reversible and Durable Aqueous Zinc-Ion Batteries. *Energy Storage Mater.* **2020**, *30*, 130−137.

(19) Yao, Z.; Wu, Q.; Chen, K.; Liu, J.; Li, C. Shallow-Layer Pillaring of a Conductive Polymer in Monolithic Grains to Drive Superior Zinc Storage via a Cascading Effect. *Energy Environ. Sci.* **2020**, *13*, 3149−3163.
(20) Dong, W.; Du, M.; Zhang, F.; Zhang, X.; Miao, Z.; Li, H.; Sang, Y.; Wang, J. J.; Liu, H.; Wang, S. In Situ Electrochemical Transformation Reaction of Ammonium-Anchored Heptavanadate Cathode for Long-Life Aqueous Zinc-Ion Batteries. *ACS Appl. Mater. Interfaces* **2021**, *13*, 5034−5043.
(21) Chen, S.; Zhang, Y.; Geng, H.; Yang, Y.; Rui, X.; Li, C. C. Zinc Ions Pillared Vanadate Cathodes by Chemical Pre-Intercalation Towards Long Cycling Life and Low-Temperature Zinc Ion Batteries. *J. Power Sources* **2019**, *441*, 227192.
(22) Yang, G.; Wei, T.; Wang, C. Self-Healing Lamellar Structure Boosts Highly Stable Zinc-Storage Property of Bilayered Vanadium Oxides. *ACS Appl. Mater. Interfaces* **2018**, *10*, 35079−35089.
(23) Tang, B.; Zhou, J.; Fang, G.; Liu, F.; Zhu, C.; Wang, C.; Pan, A.; Liang, S. Engineering the Interplanar Spacing of Ammonium Vanadates as a High-Performance Aqueous Zinc-Ion Battery Cathode. *J. Mater. Chem. A* **2019**, *7*, 940−945.
(24) Jiang, Y.; Wu, Z.; Ye, F.; Pang, R.; Zhang, L.; Liu, Q.; Chang, X.; Sun, S.; Sun, Z.; Hu, L. Spontaneous Knitting Behavior of 6.7-nm Thin $(NH_4)_{0.38}V_2O_5$ Nano-Ribbons for Binder-Free Zinc-Ion Batteries. *Energy Storage Mater.* **2021**, *42*, 286−294.
(25) Zong, Q.; Du, W.; Liu, C.; Yang, H.; Zhang, Q.; Zhou, Z.; Atif, M.; Alsalhi, M.; Cao, G. Enhanced Reversible Zinc Ion Intercalation in Deficient Ammonium Vanadate for High-Performance Aqueous Zinc-Ion Battery. *Nano-Micro Lett.* **2021**, *13*, 116.
(26) Fan, Z.; He, W.; Ni, M.; Zhang, P.; Tian, W.; Zhang, W.; Pan, L.; Sun, Z. Recent Developments of Preintercalated Cathodes for Rechargeable Aqueous Zn-Ion Batteries. *Energy Technol.* **2021**, *9*, 2000829.
(27) Tian, M.; Liu, C.; Zheng, J.; Jia, X.; Jahrman, E. P.; Seidler, G. T.; Long, D.; Atif, M.; Alsalhi, M.; Cao, G. Structural Engineering of Hydrated Vanadium Oxide Cathode by K^+ Incorporation for High-Capacity and Long-Cycling Aqueous Zinc Ion Batteries. *Energy Storage Mater.* **2020**, *29*, 9−16.
(28) Yang, W.; Dong, L.; Yang, W.; Xu, C.; Shao, G.; Wang, G. 3D Oxygen-Defective Potassium Vanadate/Carbon Nanoribbon Networks as High-Performance Cathodes for Aqueous Zinc-Ion Batteries. *Small Methods* **2020**, *4*, 1900670.
(29) He, D.; Peng, Y.; Ding, Y.; Xu, X.; Huang, Y.; Li, Z.; Zhang, X.; Hu, L. Suppressing the Skeleton Decomposition in Ti-Doped $NH_4V_4O_{10}$ for Durable Aqueous Zinc Ion Battery. *J. Power Sources* **2021**, *484*, 229284.
(30) Li, Q.; Rui, X.; Chen, D.; Feng, Y.; Xiao, N.; Gan, L.; Zhang, Q.; Yu, Y.; Huang, S. A High-Capacity Ammonium Vanadate Cathode for Zinc-Ion Battery. *Nano-Micro Lett.* **2020**, *12*, 67.
(31) Li, H.; Yang, J.; Cheng, J.; He, T.; Wang, B. Flexible Aqueous Ammonium-Ion Full Cell with High Rate Capability and Long Cycle Life. *Nano Energy* **2020**, *68*, 104369.
(32) Zhang, J.; Wang, M.; Zeng, M.; Li, X.; Chen, L.; Yang, Z.; Chen, J.; Guo, B.; Ma, Z.; Li, X. Sulfite Modified and Ammonium Ion Intercalated Vanadium Hydrate with Enhanced Redox Kinetics for Aqueous Zinc Ion Batteries. *J. Power Sources* **2021**, *496*, 229832.
(33) Kim, J.; Lee, S. H.; Park, C.; Kim, H. S.; Park, J. H.; Chung, K. Y.; Ahn, H. Controlling Vanadate Nanofiber Interlayer via Intercalation with Conducting Polymers: Cathode Material Design for Rechargeable Aqueous Zinc Ion Batteries. *Adv. Funct. Mater.* **2021**, *31*, 2100005.
(34) Tang, B.; Fang, G.; Zhou, J.; Wang, L.; Lei, Y.; Wang, C.; Lin, T.; Tang, Y.; Liang, S. Potassium Vanadates with Stable Structure and Fast Ion Diffusion Channel as Cathode for Rechargeable Aqueous Zinc-Ion Batteries. *Nano Energy* **2018**, *51*, 579−587.
(35) Du, Y.; Wang, X.; Sun, J. Tunable Oxygen Vacancy Concentration in Vanadium Oxide as Mass-Produced Cathode for Aqueous Zinc-Ion Batteries. *Nano Res.* **2021**, *14*, 754−761.
(36) Liu, S.; Yin, Y.; Ni, D.; Hui, K. S.; Hui, K. N.; Lee, S.; Ouyang, C.-Y.; Jun, S. C. Phosphorous-Containing Oxygen-Deficient Cobalt Molybdate as an Advanced Electrode Material for Supercapacitors. *Energy Storage Mater.* **2019**, *19*, 186−196.
(37) He, T.; Ye, Y.; Li, H.; Weng, S.; Zhang, Q.; Li, M.; Liu, T.; Cheng, J.; Wang, X.; Lu, J.; Wang, B. Oxygen-Deficient Ammonium Vanadate for Flexible Aqueous Zinc Batteries with High Energy Density and Rate Capability at −30 °C. *Mater. Today* **2021**, *43*, 53−61.
(38) Wang, L.; Cao, Z.; Zhuang, P.; Li, J.; Chu, H.; Ye, Z.; Xu, D.; Zhang, H.; Shen, J.; Ye, M. Electrochemical Injection Oxygen Vacancies in Layered $Ca_2Mn_3O_8$ for Boosting Zinc-Ion Storage. *ACS Appl. Mater. Interfaces* **2021**, *13*, 13338−13346.
(39) Bi, W.; Gao, G.; Wu, G.; Atif, M.; AlSalhi, M. S.; Cao, G. Sodium Vanadate/PEDOT Nanocables Rich with Oxygen Vacancies for High Energy Conversion Efficiency Zinc Ion Batteries. *Energy Storage Mater.* **2021**, *40*, 209−218.
(40) Zheng, Y.; Yao, Z.; Shadike, Z.; Lei, M.; Liu, J.; Li, C. Defect-Concentration-Mediated T-Nb_2O_5 Anodes for Durable and Fast-Charging Li-Ion Batteries. *Adv. Funct. Mater.* **2021**, 2107060.
(41) He, T.; Weng, S.; Ye, Y.; Cheng, J.; Wang, X.; Wang, X.; Wang, B. Cation-Deficient $Zn_{0.3}(NH_4)_{0.3}V_4O_{10}{\cdot}0.91H_2O$ for Rechargeable Aqueous Zinc Battery with Superior Low- Temperature Performance. *Energy Storage Mater.* **2021**, *38*, 389−396.
(42) Chen, H.; Huang, J.; Tian, S.; Liu, L.; Qin, T.; Song, L.; Liu, Y.; Zhang, Y.; Wu, X.; Lei, S.; Peng, S. Interlayer Modification of Pseudocapacitive Vanadium Oxide and $Zn(H_2O)_n^{2+}$ Migration Regulation for Ultrahigh Rate and Durable Aqueous Zinc-Ion Batteries. *Adv. Sci.* **2021**, *8*, 2004924.
(43) Zhu, T.; Mai, B.; Hu, P.; Liu, Z.; Cai, C.; Wang, X.; Zhou, L. Ammonium Ion and Structural Water Co-Assisted Zn^{2+} Intercalation/De-Intercalation in $NH_4V_4O_{10}{\bullet}0.28H_2O$. *Chin. J. Chem.* **2021**, *39*, 1885−1890.
(44) Jiang, H.; Zhang, Y.; Pan, Z.; Xu, L.; Zheng, J.; Gao, Z.; Hu, T.; Meng, C.; Wang, J. $NH_4V_3O_8{\cdot}0.5H_2O$ Nanobelts with Intercalated Water Molecules as a High Performance Zinc Ion Battery Cathode. *Mater. Chem. Front.* **2020**, *4*, 1434−1443.
(45) Zhang, Y.; Jiang, H.; Xu, L.; Gao, Z.; Meng, C. Ammonium Vanadium Oxide $(NH_4)_2V_4O_9$ Sheets for High Capacity Electrodes in Aqueous Zinc Ion Batteries. *ACS Appl. Energy Mater.* **2019**, *2*, 7861−7869.
(46) Liu, Y.; Wu, X. Hydrogen and Sodium Ions Co-Intercalated Vanadium Dioxide Electrode Materials with Enhanced Zinc Ion Storage Capacity. *Nano Energy* **2021**, *86*, 106124.
(47) Zhang, F.; Sun, X.; Du, M.; Zhang, X.; Dong, W.; Sang, Y.; Wang, J.; Li, Y.; Liu, H.; Wang, S. Weaker Interactions in Zn^{2+} and Organic Ion-Pre-Intercalated Vanadium Oxide toward Highly Reversible Zinc-ion Batteries. *Energy Environ. Mater.* **2021**, *4*, 620−630.
(48) Islam, S.; Alfaruqi, M. H.; Putro, D. Y.; Soundharrajan, V.; Sambandam, B.; Jo, J.; Park, S.; Lee, S.; Mathew, V.; Kim, J. K^+ Intercalated V_2O_5 Nanorods with Exposed Facets as Advanced Cathodes for High Energy and High Rate Zinc-Ion Batteries. *J. Mater. Chem. A* **2019**, *7*, 20335−20347.
(49) Wang, M.; Zhang, J.; Zhang, L.; Li, J.; Wang, W.; Yang, Z.; Zhang, L.; Wang, Y.; Chen, J.; Huang, Y.; Mitlin, D.; Li, X. Graphene-Like Vanadium Oxygen Hydrate (VOH) Nanosheets Intercalated and Exfoliated by Polyaniline (PANI) for Aqueous Zinc-Ion Batteries (ZIBs). *ACS Appl. Mater. Interfaces* **2020**, *12*, 31564−31574.
(50) Bin, D.; Huo, W.; Yuan, Y.; Huang, J.; Liu, Y.; Zhang, Y.; Dong, F.; Wang, Y.; Xia, Y. Organic-Inorganic-Induced Polymer Intercalation into Layered Composites for Aqueous Zinc-Ion Battery. *Chem.* **2020**, *6*, 968−984.
(51) Li, S.; Liu, Y.; Zhao, X.; Cui, K.; Shen, Q.; Li, P.; Qu, X.; Jiao, L. Molecular Engineering on MoS_2 Enables Large Interlayers and Unlocked Basal Planes for High-Performance Aqueous Zn-Ion Storage. *Angew. Chem., Int. Ed.* **2021**, *60*, 20286−20293.
(52) Qiu, N.; Yang, Z.; Xue, R.; Wang, Y.; Zhu, Y.; Liu, W. Toward a High-Performance Aqueous Zinc Ion Battery: Potassium Vanadate Nanobelts and Carbon Enhanced Zinc Foil. *Nano Lett.* **2021**, *21*, 2738−2744.

https://doi.org/10.1021/acsnano.1c11169
ACS Nano 2022, 16, 4588−4598

(53) Wan, F.; Hao, Z.; Wang, S.; Ni, Y.; Zhu, J.; Tie, Z.; Bi, S.; Niu, Z.; Chen, J. A Universal Compensation Strategy to Anchor Polar Organic Molecules in Bilayered Hydrated Vanadates for Promoting Aqueous Zinc-Ion Storage. *Adv. Mater.* **2021**, *33*, 2102701.
(54) Shan, L.; Wang, Y.; Liang, S.; Tang, B.; Yang, Y.; Wang, Z.; Lu, B.; Zhou, J. Interfacial Adsorption-Insertion Mechanism Induced by Phase Boundary Toward Better Aqueous Zn-Ion Battery. *InfoMat* **2021**, *3*, 1−9.
(55) Qin, R.; Wang, Y.; Zhang, M.; Wang, Y.; Ding, S.; Song, A.; Yi, H.; Yang, L.; Song, Y.; Cui, Y.; Liu, J.; Wang, Z.; Li, S.; Zhao, Q.; Pan, F. Tuning Zn^{2+} Coordination Environment to Suppress Dendrite Formation for High-Performance Zn-Ion Batteries. *Nano Energy* **2021**, *80*, 105478.
(56) Cui, F.; Wang, D.; Hu, F.; Yu, X.; Guan, C.; Song, G.; Xu, F.; Zhu, K. Deficiency and Surface Engineering Boosting Electronic and Ionic Kinetics in $NH_4V_4O_{10}$ for High-Performance Aqueous Zinc-Ion Battery. *Energy Storage Mater.* **2022**, *44*, 197−205.
(57) Zhang, Z.; Xi, B.; Wang, X.; Ma, X.; Chen, W.; Feng, J.; Xiong, S. Oxygen Defects Engineering of $VO_2{\cdot}xH_2O$ Nanosheets via In Situ Polypyrrole Polymerization for Efficient Aqueous Zinc Ion Storage. *Adv. Funct. Mater.* **2021**, *31*, 2103070.
(58) Geng, H.; Cheng, M.; Wang, B.; Yang, Y.; Zhang, Y.; Li, C. C. Electronic Structure Regulation of Layered Vanadium Oxide via Interlayer Doping Strategy toward Superior High-Rate and Low-Temperature Zinc-Ion Batteries. *Adv. Funct. Mater.* **2020**, *30*, 1907684.
(59) Wang, X.; Wang, Y.; Jiang, Y.; Li, X.; Liu, Y.; Xiao, H.; Ma, Y.; Huang, Y. y.; Yuan, G. Tailoring Ultrahigh Energy Density and Stable Dendrite-Free Flexible Anode with $Ti_3C_2T_x$ MXene Nanosheets and Hydrated Ammonium Vanadate Nanobelts for Aqueous Rocking-Chair Zinc Ion Batteries. *Adv. Funct. Mater.* **2021**, *31*, 2103210.
(60) Liu, Y.; Xiao, X.; Liu, X.; Cui, L. L.; Gong, Y. Aluminium Vanadate with Unsaturated Coordinated V Centers and Oxygen Vacancies: Surface Migration and Partial Phase Transformation Mechanism in High Performance Zinc-Ion Batteries. *J. Mater. Chem. A* **2022**, *10*, 912−927.
(61) Zhu, K.; Wu, T.; van den Bergh, W.; Stefik, M.; Huang, K. Reversible Molecular and Ionic Storage Mechanisms in High-Performance $Zn_{0.1}V_2O_5{\cdot}nH_2O$ Xerogel Cathode for Aqueous Zn-Ion Batteries. *ACS Nano* **2021**, *15*, 10678−10688.
(62) Wu, Z.; Lu, C.; Ye, F.; Zhang, L.; Jiang, L.; Liu, Q.; Dong, H.; Sun, Z.; Hu, L. Bilayered $VOPO_4{\cdot}2H_2O$ Nanosheets with High-Concentration Oxygen Vacancies for High-Performance Aqueous Zinc-Ion Batteries. *Adv. Funct. Mater.* **2021**, *31*, 2106816.
(63) Ren, Z.; Sun, Y.; Yin, Y.; Zhang, J.; Ren, X.; Zhao, Y.; Liang, Z.; Huai, P.; Song, F.; Jiang, Z.; Wen, W.; Li, X.; Tai, R.; Zhu, D. Metallic V_5S_8 Microparticles with Tunnel-Like Structure for High-Rate and Stable Zinc-Ion Energy Storage. *Energy Storage Mater.* **2021**, *42*, 786−793.

https://doi.org/10.1021/acsnano.1c11169
ACS Nano 2022, 16, 4588−4598